The Cryosphere Discuss., 8, 1895–1935, 2014
www.the-cryosphere-discuss.net/8/1895/2014/
doi:10.5194/tcd-8-1895-2014

The Cryosphere Discussions
Open Access

A new approach to mapping permafrost and change incorporating uncertainties in ground conditions and climate projections

Y. Zhang[1], I. Olthof[1], R. Fraser[1], and S. A. Wolfe[2]

[1]Canada Centre for Mapping and Earth Observation, Natural Resources Canada, Ottawa, Ontario, K1A 0E4, Canada
[2]Geological Survey of Canada, Natural Resources Canada, Ottawa, Ontario, K1A 0E8, Canada

Received: 19 February 2014 – Accepted: 28 March 2014 – Published: 14 April 2014

Correspondence to: Y. Zhang (yu.zhang@nrcan.gc.ca)

Published by Copernicus Publications on behalf of the European Geosciences Union.

Abstract

Spatially detailed information on permafrost distribution and change with climate is important for land-use planning and for environmental and ecological assessments. However, the required soil and surficial geology maps in the north are coarse, and projected climate scenarios vary widely. Considering these uncertainties, we propose a new approach to mapping permafrost distribution and change by integrating remote sensing data, field measurements, and a process-based model. Land-cover types from satellite imagery are used to capture the general land conditions and to improve the resolution of existing permafrost maps. For each land-cover type, field observations are used to estimate the probability of different ground conditions. A process-based model is used to quantify the evolution of permafrost for each ground condition under three representative climate scenarios (low, medium and high warming). From the model results, the probability of permafrost occurrence and the most likely permafrost conditions are determined. We apply this approach at 20 m resolution to a large area in Northwest Territories, Canada. Mapped permafrost conditions are in agreement with field observations and other studies. The data requirements, model robustness and computation time are reasonable, and this approach may serve as a practical means to mapping permafrost and changes at high resolution in other regions.

1 Introduction

About a quarter of the land in the Northern Hemisphere is underlain by permafrost (Zhang et al., 1999). Climate in northern high latitudes has warmed at about twice the rate of the global average during the 20th century, and continued warming is projected for the 21st century (ACIA, 2004). Climate warming causes ground temperature increasing, active-layer thickening, talik formation, and thawing of permafrost (Vaughan et al., 2013). These changes have significant impacts on infrastructure foundations, hydrology, ecosystems, and feedbacks to the climate system (ACIA, 2004). Mapping the

TCD
8, 1895–1935, 2014

distribution of permafrost and its possible changes with climate are important for land-use planning, infrastructure development, ecological and environmental assessments, and modelling the climate system.

Different approaches have been used to map permafrost. Traditionally, permafrost distribution was delineated into several zones based on spatial continuity or extent, defined as the proportion of an area underlain by permafrost (Nikiforoff, 1928; Heginbottom et al., 1995; Brown et al., 1998). The most widely used permafrost maps are based on this concept (Brown et al., 1998), with boundaries usually delineated manually using mean annual air temperature, field observations, and regional physiography (Nikiforoff, 1928; Heginbottom, 1984). These maps are coarse in spatial resolution (usually without an explicit spatial resolution) with broad categories, and do not consider changes with climate. Woo et al. (1992) estimated the shift in boundaries of continuous and discontinuous permafrost in Canada by assuming a 4–5 °C increase in surface temperature across the country. Anisimov and Nelson (1997) projected changes in permafrost zones using a surface frost index, calculated as the ratio of annual degree days of freezing and thawing (Nelson and Outcalt, 1987). These maps are also very coarse and do not consider variations in ground conditions. Recently, Gruber (2012) developed a global high-resolution (30 arc-second, or < 1 km) permafrost map using relations between air temperature and probability of permafrost occurrence. Bonnaventure et al. (2012) mapped permafrost probability at 30 m resolution for a large region in western Canada using the basal temperature of snow method and extensive field observations. All these methods assume that permafrost is in equilibrium with the atmospheric climate. However, ground temperature observations show that current permafrost conditions are not in equilibrium (Osterkamp, 2005), and modelling studies show that the response of permafrost to climate warming during the 21st century will be transient and non-equilibrium (Zhang et al., 2008).

In the past two decades, process-based models have been used to quantify the impacts of climate change on permafrost conditions and their spatial distributions. Process-based models can integrate more climate and ground variables and cap-

TCD
8, 1895–1935, 2014

ture transient processes from seasonal to long-term changes, but they require more detailed input data and computation time. Most spatial modelling studies, especially at national to global scales, have been conducted at half-degree latitude/longitude or coarser spatial resolutions (e.g., Lawrence and Slater, 2005; Marchenko et al., 2008; Zhang et al., 2008). At such resolutions, it is difficult to consider detailed spatial variations in vegetation and ground conditions, and the results are not suitable for land-use planning and environmental assessments. Recently, several studies have mapped permafrost at finer spatial resolutions using medium resolution satellite images (Duchesne et al., 2008; Jafarov et al., 2012; Zhang et al., 2012, 2013). In the North, however, the required maps for soil and ground conditions are coarse, with polygons in soil and surficial geology maps usually covering more than a hundred square kilometres. The lack of detailed soil and ground information is a major source of uncertainty for high resolution permafrost mapping (Zhang et al., 2012, 2013). Another source of uncertainty is climate change projections. Projected permafrost conditions differ significantly under different climate scenarios (Anisimov and Reneva, 2006; Zhang et al., 2008, 2012, 2013; Zhang, 2013), and consequently such results are difficult for decision makers to use. In this study, we develop a new approach to mapping permafrost and change incorporating uncertainties in ground conditions and climate projections. This approach integrates remote sensing, field observations, and modelling in a practical way to map permafrost at high spatial resolution. The mapped permafrost probability is similar to the concept of the traditional permafrost zones. In the paper, we describe the methodology of the approach and demonstrate its application for a large area in northern Canada.

TCD
8, 1895–1935, 2014

2 Methodology

2.1 Approach and methods

2.1.1 A general description of the approach

Figure 1 shows the scheme of the new permafrost mapping approach. A land-cover map from satellite images is used to represent the general land conditions and to improve the spatial resolution of the final products. For each land-cover type, the probability of different ground conditions is estimated based on field observations. The evolution of permafrost was simulated using a process-based model for each ground type under three representative climate change scenarios (low, medium and high warming). From these model outputs, the probability of permafrost occurrence and the most likely permafrost conditions are determined for each land cover type. The following is the rationale and feasibility of the approach.

Climate, especially air temperature, is the dominant factor controlling the spatial distribution of permafrost at large scales (from a hundred kilometers to continental scales). However, in a small area within which the climate is somewhat similar, the spatial variation of permafrost depends primarily on the distribution of vegetation and ground conditions, including topography, snow, and drainage (e.g., Brown, 1973; Morse et al., 2012). High resolution land-cover maps developed from satellite imagery can capture some general features of soil and hydrological conditions, which can explain some of the major differences in permafrost conditions (Nelson et al., 1997; Nguyen et al., 2009). However, satellite images, especially optical images, only contain information about vegetation and near surface conditions. Therefore ground conditions within a land-cover type developed by satellite images can vary substantially. For example, hollows and hummocks are common at local scales, and there are also topographically controlled variations at large scales. Such differences can cause significant variations in permafrost conditions (Duguay et al., 2005; Zhang et al., 2013). Field observations show that organic layer thickness (OLT) on the top of the mineral soil, including mosses

TCD
8, 1895–1935, 2014

and lichens, is a dominant factor affecting active-layer thickness and ground temperature (e.g., Harris, 1987; Kasischke and Johnstone, 2005; Johnson et al., 2013). Model sensitivity tests also indicate that OLT is the most sensitive factor affecting active-layer thickness and ground thermal conditions (Yi et al., 2007; Zhang et al., 2012; Riseborough et al., 2013). Therefore, we used OLT to divide soil conditions into several ground-types within a land-cover typ. As current remote sensing technologies have difficulties measuring OLT, we estimated the probability distribution of OLT based on field observations for each land-cover type. Other input parameters for ground conditions, including mineral soil texture, organic matter content in mineral soils, gravel fractions, drainage parameters, and snow-drifting parameters, can be estimated based on land-cover features, field observations, and soil and surficial geology maps. These parameters may be unique for each ground-type or the same for all ground-types within a land-cover type. Land-cover maps can be developed from satellite images, and the dominant vegetation types can be determined from the land-cover types. Leaf area indices (LAI) and wild fire history can also be estimated using optical satellite images.

Higher spatial resolution monthly climate data, necessary for spatial modelling, have been developed by interpolating station observations (Wang et al., 2006; McKenney et al., 2011). The temporal patterns of air temperature and precipitation can be estimated using observations at climate stations (Zhang et al., 2012, 2013) or from reanalysis of climate observations. Water vapour pressure can be estimated based on daily minimum air temperature, and daily total insolation without topographic effects can be estimated using latitude, the day of the year, the diurnal temperature range (Zhang et al., 2012). Topographical effects on solar radiation can be calculated using a digital elevation model (Zhang et al., 2013). To consider the uncertainty of future climate projections, three scenarios (low, medium and high warming) can be selected to represent the medium and general range of the probable scenarios based on climate model projections. If we assume that the low and high warming scenarios represent the lower and upper quartiles of the probable scenarios and the medium warming sce-

TCD
8, 1895–1935, 2014

nario represents the two middle quartiles, the probabilities of the low, medium and high warming scenarios would be 0.25, 0.5, and 0.25, respectively.

To map permafrost and its evolution, permafrost dynamics for each grid cell are modelled under the possible ground-types and the three representative climate scenarios. The probability of permafrost occurrence in a grid cell can be determined based on the probabilities of the ground-types and climate scenarios. In turn, the distributions of permafrost probability and the most likely permafrost conditions can be mapped. The probability of permafrost within a grid cell can be interpreted as a probability due to the uncertainties in ground conditions and climate projections, or can be interpreted as permafrost proportion or extent due to spatial heterogeneity within the grid cell, especially when the grid cell is large.

2.1.2 Estimating the probability of ground-types within land-cover types

The probability distribution of ground-types in all the areas of a land-cover type was estimated using a modified logistic function based on field sampling observations of OLT at different locations

$$F(x) = a + (1 - a)/(1 + e_x), \quad (1)$$

where x is OLT (cm), and $F(x)$ is the cumulative distribution probability of OLT for a land-cover type. a is a parameter to modify the standard logistic function (no unit, and $a < 1$). e_x is an exponential function of x

$$e_x = \exp[-(x - \mu)/s], \quad (2)$$

where μ and s are the average and the standard deviation of the distribution (all in centimetres). Since OLT and cumulative distribution probability cannot be negative, the domain of x will be $x \geq x_0$, where

$$x_0 = \begin{cases} 0 & (a \geq 0) \\ \mu - s\ln(-1/a) & (a < 0). \end{cases} \quad (3)$$

TCD
8, 1895–1935, 2014

The probability density function can be derived by differentiating Eq. (1). We divided the probability density function by $1 - F(x_0)$ so that the total probability equals 1 when $x \geq x_0$.

$$f(x) = \frac{(1-a)e_x}{s(1+e_x)^2[1-F(x_0)]}, \quad (4)$$

where $f(x)$ is the probability density function. $F(x_0)$ is determined by Eq. (1) when $x = x_0$.

The probability of a ground-type i can be determined using Eq. (4)

$$p(i) = \int_{a_i}^{b_i} f(x)\mathrm{d}x = \left(1 + 1/e_{x_0}\right)\left[1/\left(1+e_{b_i}\right) - 1/\left(1+e_{a_i}\right)\right], \quad (5)$$

where $p(i)$ is the probability of a ground-type i for OLT ranging from a_i to b_i. The values of e_{x0}, e_{a_i}, and e_{b_i} are calculated from Eq. (2) when x equals x_0, a_i, and b_i, respectively. The value of i ranges from 1 to N, where N is the number of ground-types. The thinnest and thickest OLT ground-types can be determined from Eq. (5) using a predetermined probability level. Then, the OLT ranges of the other ground-types can be defined. The three parameters in Eq. (1) (a, μ and s) can be determined by comparing the fitted cumulative probability with the observed relative cumulative frequency. Figure 2 shows an example of distribution of ground-types in a land-cover type. For the model input, the OLT of a ground-type was represented by $0.5(a_i + b_i)$, except for the thinnest and thickest OLT ground-types, which were estimated as the OLT at which the probability densities equal $0.5[f(x_0)+f(b_1)]$ and $0.5f(a_N)$, respectively.

Sensitivity tests showed that the modelled average permafrost conditions converged quickly with the increase in the number of ground-types. Permafrost conditions between two ground-types were similar when the difference of their OLT was less than 5 cm, especially when OLT was thicker than 30 cm, and permafrost was not sensitive to the

TCD
8, 1895–1935, 2014

changes in OLT when OLT was thicker than 50 cm (Zhang et al., 2012; Riseborough et al., 2013). Based on this response pattern we can select the thickness and the number of ground-types.

2.1.3 The model

The permafrost condition and its changes with climate for each ground-type were quantified using the Northern Ecosystem Soil Temperature model (NEST). NEST is a one-dimensional transient model that considers the effects of climate, vegetation, snow, and soil conditions on ground thermal dynamics based on energy and mass transfer through the soil-vegetation-atmosphere system (Zhang et al., 2003). Ground temperature is calculated by solving the one-dimensional heat conduction equation. The dynamics of snow depth, snow density and their effects on ground temperature are considered. Soil water dynamics are simulated considering water input (rainfall and snowmelt), output (evaporation and transpiration), and distribution among soil layers. Soil thawing and freezing, and associated changes in fractions of ice and liquid water, are determined based on energy conservation. Detailed description of the model and validations can be found in Zhang et al. (2003, 2005, 2006). Lateral flows and snow drifting are parameterized in a simplified way (Zhang et al., 2002, 2012). The model can also consider the effects of topography on solar radiation (Zhang et al., 2013).

2.2 Applying the approach to an area in northern Canada

2.2.1 Study area and field observations

We applied this approach to a 94 km by 94 km area in Northwest Territories, Canada, centred at 62.77° N, 114.27° W (Fig. 3a). The area is located in the Great Slave Geological Province, a region of high mineral resource development in northern Canada, where seasonal and all-weather roads and other infrastructure are important. With the effects of the last glacial ice sheet and the glacial lake McConnell, most of the surficial

TCD
8, 1895–1935, 2014

geology consists of fine-grained glaciolacustrine sediments and wave-washed bedrock (Wolfe et al., 2013). The study area includes the Great Slave Lowlands and Uplands with vegetation ranging from dense forest to arctic tundra (Ecological Classification Group, 2007). The Great Slave Lowlands are poorly-drained low relief terrain characterized by numerous water bodies separated by fens, peatlands, mixed woodlands, white birch (*Betula papyrifera*) and black spruce (*Picea mariana*) forests, while the Uplands are areas of higher relief and bedrock outcrops. Permafrost in the region is discontinuous and highly variable, usually with abrupt transitions from frozen to unfrozen ground over short distances (Wolfe et al., 2011). Therefore it is important to provide spatially detailed information about permafrost conditions and possible changes with climate warming. We selected this area also because it covers a large spatial environmental and vegetation gradient and many field observations are available. In this area, the thirty-year (1971–2000) mean annual air temperature ranged from −6.9 °C to −4.9 °C (Fig. 3f), and mean annual total precipitation ranged from 288 mm to 309 mm. Monthly mean air temperature varied from −29 °C in January to 16 °C in July.

We conducted fieldwork in this area in 2005 and 2011. Data were collected on land-cover types, vegetation conditions, surface OLT, and soil profile conditions (depths of the horizons, texture and organic matter content), drainage, and summer thaw depths. We also collected observations made by other investigators in this area (Gaanderse, 2011; Brown, 1973; Karunaratne et al., 2008; Roujanski et al., 2012). In total, we compiled 124 observation sites (Fig. 3b). Most sites were located near roads in the south providing easy access. Wolfe et al. (2014) also identified 1777 lithalsas in the Great Slave Lowlands and Uplands using 1 : 60 000 scale aerial photos acquired between 1978 and 1980, in which 955 sites were within our study area (Fig. 3b). Lithalsas are permafrost mounds formed by ice segregation within mineral soil. These field data and lithalsa observations were used to validate the modelled permafrost distribution.

TCD
8, 1895–1935, 2014

2.2.2 Land-cover types and the probability of ground-types

The land-cover types (Fig. 3c) were classified using SPOT High-Resolution Visible and Infrared images. The area is covered by a SPOT 4 image acquired on 7 August 2008 and a SPOT 5 image from 4 August 2011, both at 20 m spatial resolution. Radiometric normalization was performed using robust Theil-Sen regression on the overlap between the two scenes to adjust the 2008 radiometry to match the 2011 image. The Enhancement Classification Method (Beaubien et al., 1999) was used to improve image contrast by stretching the dynamic range representing land features to the full 8-bit dynamic range while compressing water, cloud and shadow. A large number of spectral clusters were generated from the enhanced multispectral data using fuzzy *k*-means clustering and applying a pseudo-colour table to represent the enhanced colours. The Classification by Progressive Generalization approach (Cihlar et al., 1998) was used to manually merge and label clusters to 16 land-cover types considering spectral similarity and spatial proximity to depict land-cover features visible in high resolution images in Google Earth™ and our field data. Validation of a national land-cover product (Olthof et al., 2013) that includes this study area suggests an overall accuracy in the range of 70 %. We modelled permafrost conditions for 13 land-cover types, which exclude water, roads and recently disturbed areas (Table 1).

We estimated the probability distribution of the ground-types in each land-cover type using field observations of OLT. Most of the land-cover types had five to eight ground-types (Table 2). Rock outcrop was assumed as one ground-type without organic layer. The parameters were determined by fitting the observed relative cumulative frequency with the modified logistic function (Table 2). Our field observations in the study area did not include land-cover types of erect shrubs, shrub-herb mixture and herbs (types S, SH and H, respectively). To fill this data gap, we used field observations of these land-cover types that were conducted in 2013 near Tuktoyaktuk (69.44° N, 133.03° W) and Fort McPherson (67.44° N, 134.88° W).

TCD
8, 1895–1935, 2014

2.2.3 Leaf area indices and fire disturbances

Leaf area indices in mid-summer (Fig. 3d) were mapped using Landsat-5 imagery (acquired on 21 July 2002) based on Abuelgasim and Leblanc (2011), who developed an equation of LAI using field observations and the reduced simple ratio index of Landsat channels 3, 4 and 5. As they normalized their Landsat scenes based on SPOT VGT composite in the summer of 2005, we first normalized our Landsat images to the same SPOT VGT composite and then calculated LAI using their LAI equation.

A digital database of historically burned areas and year of burning (Fig. 3e) was obtained from the Government of Northwest Territories Centre for Geomatics (http://www.geomatics.gov.nt.ca/). In the study area, about 26.2 % of the land area experienced wildfire since 1967. The major fires were in 1973 and 1998, which accounted for 71.6 % and 19.3 % of the total burned area, respectively. Fires consume vegetation and soil organic matter. The amount of consumption and the post-fire regeneration process depend on fire intensity, vegetation condition, soil moisture and local topography (Turetsky et al., 2011). For simplicity, we assumed that fires consumed all the foliage, and the remaining standing woody parts had little effect on radiation and surface energy exchanges. The albedo of the land surface in snow-free period was reduced by 50 % immediately after the fire (Yoshikawa et al., 2003; Mack et al., 2011). We assumed that fire could consume a maximum of 13 cm of mosses and top organic matter except for wetland and fen (type W), where we used half of this depth due to their wet conditions (Johnestone et al., 2010; Turetsky et al., 2011).

Although trees can take several decades to re-establish, the regeneration and re-establishment of sedges and shrubs occur rapidly (Bond-Lamberty et al., 2002). Based on the LAI map for this area (representing the conditions in 2002), the average LAI in the area burned after 1994 (mostly in 1998) was about 60 % of the average LAI in the non-burned area, and the average LAI in the area burned before 1973 was about 120 % of the non-burned area. Based on these results and other studies (Bond-Lamberty et al., 2002), we assumed that land-cover types dominated by sedges and shrubs

TCD
8, 1895–1935, 2014

would regenerate in the following year after a fire and LAI would reach pre-burn levels in 5 and 15 years, respectively. Tree-dominated land types would regenerate in 5 years after a fire and LAI would reach pre-burn level in 50 years. We also assumed that the surface organic matter and mosses consumed by fire would recover in 50 years (Mack et al., 2011). The albedo of the land surface would also return to the pre-burn level. The increases in LAI, albedo and surface organic layer were treated as linear patterns with time after regeneration. After recovery, the land-cover types will be the same as pre-burn conditions, and summer LAI will not change with time (LAI varies seasonally). We did not consider new fires after 2013.

2.2.4 Climate data

The 5 arc-minutes (about 10 km) spatial 30 year averages (1971–2000) of monthly air temperature (Fig. 3f) and precipitation were from McKenney et al. (2012). The data were interpolated from station observations. We interpolated these monthly data to 20 m resolution using bi-linear interpolation, and annual total degree days for air temperatures above 0 °C were calculated. Based on annual total degree days and annual total precipitation, the climate was clustered into 20 classes. The average relative errors were 0.25 % and 0.45 % for the annual total degree days and annual total precipitation, respectively. Temporal climate changes were estimated using daily observations at the Yellowknife airport climate station as a template. A detailed description of the method can be found at Zhang et al. (2013). From the 1940s to the recent past decade (2003–2012), annual mean air temperature increased by 2.1 °C. The increase mainly occurred after the mid-1960s. Annual total precipitation increased by 99 mm from the 1940s to the past decade.

We selected three climate change scenarios from various climate projections of different climate models and greenhouse gas emissions. The climate scenario data were downloaded from the World Data Center for Climate (http://mud.dkrz.de/wdc-for-climate/ accessed in April 2011). The selected low, medium and high warming scenarios were generated by CCCma (B1), CCCma (A1B) and MIROC (A1B), respec-

TCD
8, 1895–1935, 2014

tively (Fig. 4). Under these three scenarios, air temperature is projected to increase 0.4, 1.7 and 2.7 °C, respectively, from the recent past decade to the 2050s; and to increase 1.0, 3.4 and 4.9 °C, respectively, from the recent past decade to the 2090s. The projected changes in precipitation are not very significant (Fig. 4b).

2.2.5 Other input parameters

In addition to OLT, the model also requires inputs about mineral soil conditions and hydrological parameters. Field surveys and coring indicate differences in sediment types above and below an elevation of about 205 m above sea level (a.s.l.), likely related to sedimentation within the glacial lake McConnell (Stevens et al., 2012). Therefore, we first divided the study area into two regions using the 205 m a.s.l. isoline (Fig. 3b) and then defined the mineral soil conditions for each region. This delineation also closely corresponds to the separation of the Great Slave Lowlands and Uplands (Ecological Classification Group, 2007). At elevations below 205 m, mineral soils are mainly composed of clay (Wolfe et al., 2011). Above 205 m, mineral soils were assigned as sandy loam for the low-vegetation or barren land (type L) and low- to medium-density coniferous forest (type C3), and as silty clay for other land-cover types based on the general patterns of field observations (Stevens et al., 2012; Wolfe et al., 2011). The organic matter content in mineral soils was estimated based on the general patterns observed by Hossain et al. (2007). Except for low vegetation and bedrock (Types L and R), the depth of all surficial deposits (including peat and mineral soils) are assumed to be 5 m based on most of the borehole observations (Wolfe et al., 2011). The soil thickness for the low vegetation type was assumed to be 2.5 m and we assumed no soil on bedrock outcrops. The thermal conductivity of bedrock was 0.026 $W m^{-1} °C^{-1}$ (Brown, 1973). The geothermal heat flux was assumed as 0.007 $W m^{-2}$ (Majorowicz and Grasby, 2010).

The model also requires several parameters to estimate lateral water flows (Zhang et al., 2002, 2012). We defined these parameters based on the general drainage conditions and the range of water table for different land-cover types (Table 3). The model

TCD
8, 1895–1935, 2014

also has a parameter to consider the effects of snow-drifting due to wind (Zhang et al., 2012). A positive value is for the fraction of snowfall drifted away from the site and a negative value for capturing some drifting snow from surroundings. We estimated this parameter based on the vegetation types and their density (represented by the LAI in summer) (Table 3). Since this region is relatively flat, we did not consider the effects of topography on solar radiation.

2.2.6 Spatial modelling

To reduce the computation time, LAI was divided into 18 levels based on the effects of LAI on solar radiation (i.e., exp(−0.5LAI)). The latitude in the area was divided into five grads (0.2° difference between two adjacent grads). Together with the land-cover types (13 types), elevation levels (2 types), climate (20 classes), and wildfire years (13 types), the land pixels in the study area had 31 724 unique combinations of the input types, which was 0.2 % of the land pixels in this area (we ran the model only for these unique input types rather than running the model pixel by pixel). For each land-cover type, the model was run for all the ground-types under the three climate scenarios. Model computations took about three weeks using three personal computers.

3 Result and analysis

3.1 Permafrost distributions

Figure 5 shows the distributions of permafrost probability modelled for the 1950s (1950–1959), the 2000s (2000–2009) and the 2050s (2050–2059). These results show significant reductions in permafrost probability due to climate warming from the 1950s to the 2050s. Permafrost is predicted to disappear completely in most of the area by the end of the 21st century. The spatial distribution of permafrost in this area was mainly related to land-cover types and associated ground conditions. For example, the non-permafrost area in the 2000s mainly occurred in rock outcrops, low vegetation, and

TCD
8, 1895–1935, 2014

deciduous forest (Land-cover types R, L and D, respectively), while sparse coniferous forest (types C4 and C5) and herb dominated areas and wetlands (types H and W) had high permafrost probability. Leaf area indices and fire disturbances also affected permafrost conditions, but their effects were mixed with that of land-cover types. Permafrost probability in the northeast corner of the study area was higher, probably due to the relatively cooler climate in this area. However, the overall effects of the climate gradient on spatial distribution of permafrost were not so obvious because of the strong effects of ground conditions and relatively small climate gradient in this area (Fig. 3f). For example, although the southern part is slightly warmer than the northern part, LAI is higher and soils contain more clay in the south, which compensated for the effects of warmer temperature on permafrost development.

Figure 6a shows the modelled temporal change of average permafrost probability (or permafrost extent) in this area from 1942 to 2100. On average, permafrost extent was reduced from 72.0 % in the 1950s to 52.0 % in the 2000s. The model predicted that permafrost extent would be reduced to 12.4 % in the 2050s and to 2.5 % in the 2090s. The difference in permafrost extent between the low and high warming scenarios was relatively small, usually less than 5 % (in permafrost extent).

Different land cover types show different decreasing patterns in permafrost extent (Fig. 6b). The most rapid reduction in permafrost extent was in low vegetation or barren land (type L) due to their exposed land conditions. The reduction was rapid in deciduous forest area (type D) due to its shallow OLT. Spruce lichen bogs and wetlands (types C5 and W) were the last land-cover types experiencing permafrost reduction. With time, the reduction of permafrost for a land-cover type generally shows a slow, rapid and slow decline pattern. The initial slow reduction is due to the lower warming rate of climate (especially before the mid of the 1980s) and the time required to warm the ground to a critical level. The later slow reduction of permafrost is related to ground-types with deep organic layers and high LAI, which can protect permafrost from thawing. Model results show that some forest areas could still maintain permafrost by

TCD
8, 1895–1935, 2014

the end of the 21st century mainly due to their deep OLT and high LAI, assuming they were not disturbed by wildfires during the 21st century.

3.2 The most likely permafrost conditions

Permafrost conditions under varying ground-types differ significantly due to the effects of OLT. Permafrost does not typically exist where OLT is very shallow. Therefore it is difficult to calculate the average permafrost conditions. A meaningful way is to present the most likely permafrost conditions, which is determined from the model results of the most likely ground-types under the medium warming climate scenario. The most likely permafrost extent averaged in this area (dashed curve in Fig. 6a) was slightly different from the average of all the ground types under the three climate scenarios (solid curve in Fig. 6a). The average and the most likely spatial patterns were similar in the 1950s and 2000s (the most likely permafrost distribution only has two types, no permafrost or with permafrost, shown respectively as white or other colours in Fig. 7). The average and the most likely permafrost distributions were very different in the 2050s (comparing Figs. 5c and 7c) as permafrost will disappear in most areas under the most probable ground and climate conditions.

Figure 7 shows the distribution of the most likely active-layer thicknesses in the 1950s, 2000s and 2050s. Active layer becomes deeper from the 1950s to the 2000s, and permafrost in most areas will disappear in the 2050s. The red patches (deeper active layer) in the northeastern corner in Fig. 7b are due to the effects of wildfires, which consumed vegetation and some of the top organic matters. For the pixels with permafrost in all the years before 2012, the average active-layer thickness increased from 0.7 m in the 1940s to 1.4 m in the 2000s.

3.3 Result validation

According to the Canada permafrost map (Heginbottom et al., 1995), the study area is within the extensive discontinuous permafrost zone. Based on the 124 observation

TCD
8, 1895–1935, 2014

sites in this area, permafrost was detected at 87 sites. Frozen ground was not detected at the other 37 sites. The permafrost sites account for 70.2 % of the observation sites, which confirm that this area is within the extensive discontinuous permafrost zone (50–90 %). The modelled average permafrost extent in this area was 64.2 % during 1942–2012, well within the range of the extensive discontinuous zone. Based on the ground-types most closely matching local conditions, the model results show that permafrost occurred at 71 of 87 observed permafrost sites. For the other 37 sites where no frozen ground was detected in the field, the model results show that 21 sites did not have permafrost, six sites had permafrost but their thaw depths were deeper than the measurement depths, and the model results were incorrect for the other ten sites. Overall, the model correctly simulated permafrost occurrence for 82 % of the observed permafrost sites, and correctly simulated 73 % of the sites where frozen ground was not detected in the field either because thaw depths were deep, or permafrost did not exist. Coincidently, the modelled and observed total numbers of sites with permafrost (87 sites) were the same.

Figure 8a shows a comparison between the modelled and observed percentage of sites with permafrost at each land-cover type. The model results were close to the observations for most of the land-cover types except for the low vegetation sites (L). Permafrost was observed at three of the four low vegetation sites whereas the model did not indicate permafrost at these sites. Field data show that two sites are in disturbed areas with some peat layers added in the soil profile and another site is near the road with some embankment material on the surface. These modified conditions may have actually promoted permafrost development.

Wolfe et al. (2014) identified 955 lithalsas in our study area (Fig. 3b). By definition, permafrost exists at these locations. We calculated the average permafrost probability during 1978–1980, at which time the aerial photographs were acquired to identify the lithalsas. Eighteen locations were classified as water since they are very close to water bodies. The model results show that all the 937 non-water locations have a ≥ 14 % probability of permafrost occurrence. The probability of permafrost occur-

TCD
8, 1895–1935, 2014

rence was ≥ 50 % at 838 locations (89.4 % of the locations), and was ≥ 90 % at 501 locations (53.5 % of the locations). The average probability was 76.9 % for all the locations. The lithalsa mounds are usually well drained due to their local topography and contain segregation ice. The modelled did not consider these factors therefore they might contribute to the underestimation of the probability of permafrost occurrence for these locations.

The modelled mean summer thaw depth for each land-cover type was comparable with the observations although the variation range was usually large among the sites (Fig. 8b). The modelled average thaw depth of all the sites with permafrost was 0.78 m, which was very close to the average of the observations (0.81 m). Figure 9 shows a scatter graph comparison for the 71 sites with permafrost. The magnitudes of the modelled summer thaw depths were similar to the observations for most of the sites although significant differences existed for some sites due to their specific soil, vegetation and hydrological conditions. The correlation coefficient is 0.365 (n = 71).

The modelled permafrost thickness for recent decades ranged from several meters to 130 m, which is comparable with the observations reported by Smith and Burgess (2002) and Roujanski et al. (2012). We also tested the model offline using observations in this area measured by Brown (1973), Karunaratne et al. (2008), and Roujanski et al. (2012). Based on their local ground and vegetation conditions, the model could capture their ground temperature regimes and permafrost conditions. The modelled dynamics of snow depth, especially the timing of accumulation and disappearance of snow and the maximum snow depth, compared well with the observations at the Yellowknife climate station. The correlation coefficient is 0.892 for the 19 794 observations from the 1955 to 2012.

4 Discussion

This study proposes a new approach for mapping permafrost and change with climate considering uncertainties in ground conditions and climate projections. We apply this

TCD
8, 1895–1935, 2014

approach at 20 m resolution to a large area in northern Canada. The data requirement and the cost of computation are reasonable, and the mapped permafrost conditions are in reasonable agreement with field observations and other studies. Compared to previous equilibrium and coarse resolution mapping methods, several features of this approach are noteworthy.

First, this approach integrates satellite remote sensing data, field observations, and a process-based model for mapping permafrost and changes. Satellite data can greatly improve the spatial resolution of existing permafrost maps, and can provide various parameters including land-cover, LAI, wildfire, and topographic features. As current soil and surficial geological maps are coarse, the heterogeneous ground conditions are statistically represented based on field observations. Three climate scenarios are selected to represent the medium and range of probable future climate changes. Based on interactions of climate, snow-pack, vegetation, and ground conditions, the process-based model quantifies permafrost conditions and transient changes from seasons to centuries.

Second, the produced permafrost maps by this approach are more useful for land-use planners and decision-makers due to their higher spatial resolution and consideration of climate change effects. These maps also incorporated incomplete and uncertain information about ground conditions and future climate projections. Previous studies usually presented different permafrost maps under assumed different ground conditions and climate change scenarios (e.g., Zhang, 2013; Zhang et al., 2008, 2013; Daanen et al., 2011). Such maps are difficult to use due to their wide differences. This approach used a concept of probability, which is similar to the traditional permafrost maps. However, the new maps have a much higher degree of precision and spatial resolution than the traditional permafrost maps. Figure 10 shows the importance of spatial resolution for permafrost zones. At 20 km resolution, our results show the same permafrost zone as in the traditional permafrost map (extensive discontinuous). At finer resolutions, however, other permafrost zones appeared. In addition, this approach also

TCD
8, 1895–1935, 2014

provides most likely permafrost conditions, such as active-layer thickness and permafrost thickness.

Third, this approach may serve as a practical way to map permafrost evolution at high spatial resolution for other regions. Satellite remote sensing data are routinely available across the globe. To consider the heterogeneity of ground conditions, we estimated their statistical distributions rather than mapping ground conditions explicitly, which is difficult at present. Organic layer thickness and other general ground conditions can be surveyed in the field and the data can be accumulated gradually as they do not change significantly with time without disturbances. In this study, we estimated the probability of ground-types based on OLT. With more field data available, other ground features can be included to better define ground-types. The spatial input data can be organized and used to run the model on multiple computers simultaneously, thus greatly reducing computation time for high resolution spatial modelling. In addition, this approach allows for changes or improvement in spatial resolution, new development in the model and remote sensing technology, and with the availability of more field observations.

Although we considered snow drifting and lateral water flows, the NEST model is still one-dimensional and assumes each grid cell to be uniform without lateral heat exchange. Therefore, the results cannot represent areas with strong lateral heat fluxes, such as areas between very different land-cover types, especially close to water bodies. In this study, we considered fire disturbances occurred in the past, but we did not consider future fires. Such a treatment might over-estimate future permafrost extent because high LAI and deep organic layer can effectively keep permafrost in disequilibrium from the warming of the atmospheric climate (Camill and Clark, 1998). And finally, this study did not consider changes in land-cover types and LAI with climate warming. Observations show that northern high latitudes are becoming greener and shrubbier with climate warming (e.g., Tape et al., 2006). These changes can be very important for the evolution of permafrost.

TCD
8, 1895–1935, 2014

5 Conclusions

Spatially detailed information about permafrost evolution with climate warming is important for land-use planning and for environmental and ecological assessments. Although satellite remote sensing can provide detailed maps of vegetation and land-cover types, knowledge regarding soil and ground conditions are much coarser, which greatly limits our capacity to map permafrost at relatively high resolutions. The wide range of projected climate scenarios also brings in uncertainties for mapping permafrost change. Our proposed new approach incorporates these uncertainties for permafrost mapping by integrating remote sensing, field observations, and a process-based model. Land-cover types from satellite remote sensing are used to capture the general land features and to improve the spatial resolution of existing permafrost maps. Other vegetation features can also be derived from remote sensing imagery. The probability of different ground conditions within land-cover types is estimated from field observations. A process-based model is used to quantify the dynamics of permafrost for each ground type under three representative climate scenarios of low, medium and high warming. From the model results, the probability of permafrost occurrence and the most likely permafrost conditions are determined. We apply this approach at 20 m resolution to a large area in Canada. The mapped permafrost conditions are in agreement with field observations and other studies. This demonstrates that the data requirements, model robustness and computation time are reasonable, and that this approach may serve as a practical means to map permafrost evolution at a high resolution in other regions.

Acknowledgements. The authors would like to thank Sylvain Leblanc for providing software and procedures for mapping leaf area indices, and undertaking the critical internal review of the paper. Adrian Gaanderse provided many site observations about ground conditions in the study area. The authors also thank Peter Morse for carefully reviewing the paper. This study was supported by the Climate Change Geoscience Program and Remote Sensing Science Program in Natural Resources Canada (Earth Science Sector contribution number 20130435), and Cumulative Impact Monitoring Program (CIMP) in Northwest Territories, Canada.

TCD
8, 1895–1935, 2014

References

Abuelgasim, A. A. and Leblanc, L.: Leaf area index mapping in northern Canada, Int. J. Remote Sens., 32, 5059–5076, doi:10.1080/01431161.2010.494636, 2011.

ACIA: Impact of a Warming Arctic: Arctic Climate Impact Assessment, Cambridge University Press, Cambridge, UK, 1042 pp., 2005.

Anisimov, O. A. and Nelson, F. E.: Permafrost zonation and climate change: results from transient general circulation models, Climatic Change, 35, 241–258, 1997.

Anisimov, O. and Reneva, S.: Permafrost and changing climate: the Russian perspective, Ambio, 35, 169–175, 2006.

Beaubien, J., Cihlar, J., Simard, G., and Latifovic, R.: Land cover from multiple thematic mapper scenes using a new enhancement-classification methodology, J. Geophys. Res., 104, 27909–27920, 1999.

Bond-Lamberty, B., Wang, C., Gower, S. T., and Norman, J.: Leaf area dynamics of a boreal black spruce chronosequence, Tree Physiol., 22, 993–1001, 2002.

Bonnaventure, P. P., Lewkowicz, A. G., Kremer, M., and Sawada, M. C.: A permafrost probability model for the southern Yukon and northern British Columbia, Canada, Permafrost Periglac., 23, 52–68, doi:10.1002/ppp.1733, 2012.

Brown, J., Ferrians Jr., O. J., Heginbottom, J. A., and Melnikov, E. S.: Circum-arctic map of permafrost and ground ice conditions, National Snow and Ice Data Center, Boulder, CO, Revised February 2001, Digital media, 1998.

Brown, R. J. E.: Influence of climatic and terrain factors on ground temperatures at three locations in the permafrost region in Canada, Proceedings of the second International Conference on permafrost, North American Contribution, Yakutsk, USSR, 13–18 July 1973, 27–34, 1973.

Camill, P. and Clark, J. S.: Climate change disequilibrium of boreal permafrost peatlands caused by local processes, Am. Nat., 151, 207–22, doi:10.1086/286112, 1998.

Cihlar, J., Xiao, Q., Chen, J., Beaubien, J., Fung, K., and Latifovic, R.: Classification by progressive generalization: a new automated methodology for remote sensing multichannel data, Int. J. Remote Sens., 19, 2685–2704, 1998.

Daanen, R. P., Ingeman-Nielsen, T., Marchenko, S. S., Romanovsky, V. E., Foged, N., Stendel, M., Christensen, J. H., and Hornbech Svendsen, K.: Permafrost degradation risk zone

TCD
8, 1895–1935, 2014

assessment using simulation models, The Cryosphere, 5, 1043–1056, doi:10.5194/tc-5-1043-2011, 2011.
Duchesne, C., Wright, J. F., and Ednie, M.: High-resolution numerical modeling of climate change impacts on permafrost in the vicinities of Inuvik, Norman Wells, and Fort Simpson, NT, Canada, in: Proceedings of the Ninth International Conference on Permafrost, edited by: Kane, D. L., and Hinkel, K. M., Institute of Northern Engineering, University of Alaska Fairbanks, 29 June–3 July 2008, Fairbanks, Alaska, USA, 385–390, 2008.
Duguay, C. R., Zhang, T., Leverington, D. W., Romanovsk, V. E.: Satellite remote sensing of permafrost and seasonally frozen ground, in: Remote Sensing of Northern Hydrology, Geoph. Monog. Series 163, edited by: Duguay, C. R. and Pietroniro, A., American Geophysical Union, Washington, doi:10.1029/163GM06, 91–118, 2005.
Ecosystem Classification Group: Ecological Regions on the Northwest Territories: Taiga Shield, Department of Environment and Natural Resources, Government of the Northwest Territories, Yellowknife, NT, Canada, 173 pp., 2007.
Gaanderse, A.: Seasonal thaw depths in relation to surficial characteristics in the taiga shield high boreal ecoregion surrounding Yellowknife, Northwest Territories, A theses for a Bachelor's of Arts degree, Department of Geography and Environmental Studies, Carleton University, Ottawa, Canada, 59 pp., 2011.
Gruber, S.: Derivation and analysis of a high-resolution estimate of global permafrost zonation, The Cryosphere, 6, 221–233, doi:10.5194/tc-6-221-2012, 2012.
Harris, S. A.: Influence of organic (O_f) layer thickness in active-layer thickness at two sites in the western Canadian arctic subarctic, Erdkunde, 41, 275–285, 1987.
Heginbottom, J. A.: The mapping of permafrost, Can. Geogr., 28, 78–83, 1984.
Heginbottom, J. A., Dubreuil, M. A., and Harker, P. A.: Canada – permafrost, in: National Atlas of Canada, 5th Edn., National Atlas Information Service, Natural Resources Canada, Ottawa, ON, Canada, MCR 4177, 1995.
Hossain, M. F., Zhang, Y., Chen, W., Wang, J., and Pavlic, G.: Soil organic carbon content in northern Canada: a database of field measurements and its analysis, Can. J. Soil Sci., 87, 259–268, doi:10.4141/S06-029, 2007.
Jafarov, E. E., Marchenko, S. S., and Romanovsky, V. E.: Numerical modeling of permafrost dynamics in Alaska using a high spatial resolution dataset, The Cryosphere, 6, 613–624, doi:10.5194/tc-6-613-2012, 2012.

TCD
8, 1895–1935, 2014

Johnson, K. D., Harden, J. W., McGuire, A. D., Clark, M., Yuan, F. M., and Finley, A.: Permafrost and organic layer interactions over a climate gradient in a discontinuous permafrost zone, Environ. Res. Lett., 8, 035028, doi:10.1088/1748-9326/8/3/035028, 2013.

Johnstone, J. F., Chapin III, F. S., Hollingsworth, T. N., Mack, M. C., Romanovsky, V., and Turetsky, M.: Fire, climate change, and forest resilience in interior Alaska, Can. J. Forest Res., 40, 1302–1312, doi:10.1139/X10-061, 2010.

Karunaratne, K. C., Kokelj, S. V., and Burn, C. R.: Near-surface permafrost conditions near Yellowknife, Northwest Territories, Canada, in: Proceedings of the Ninth International Conference on Permafrost, edited by: Kane, D. L., and Hinkel, K. M., Institute of Northern Engineering, University of Alaska Fairbanks, 29 June–3 July 2008, Fairbanks, Alaska, USA, 907–912, 2008.

Kasischke, E. S. and Johnstone, J. F.: Variation in postfire organic layer thickness in a black spruce forest complex in interior Alaska and its effects on soil temperature and moisture, Can. J. Forest Res., 35, 2164–2177, doi:10.1139/X05-159, 2005.

Lawrence, D. M. and Slater, A.: A projection of severe near-surface permafrost degradation during the 21st century, Geophys. Res. Lett., 32, L24401, doi:10.1029/2005GL025080, 2005.

Mack, M. C., Bret-Harte, M. S., Hollingsworth, T. N., Jandt, R. R., Schuur, E. A. G, Shaver, G. R., Verbyla, D. L.: Carbon loss from an unprecedented Arctic tundra wildfire, Nature, 475, 489–492, doi:10.1038/nature10283, 2011.

Majorowicz, J. and Grasby, S. E.: Heat flow, depth-temperature variations and stored thermal energy for enhanced geothermal systems in Canada, J. Geophys. Eng., 7, 232–241, doi:10.1088/1742-2132/7/3/002, 2010.

Marchenko, S., Romanovsky, V., and Tipenko, G.: Numerical modeling of spatial permafrost dynamics in Alaska, in: Proceedings of the Ninth International Conference on Permafrost, edited by: Kane, D. L. and Hinkel, K. M., Institute of Northern Engineering, University of Alaska, Fairbanks, Alaska, USA, 29 June–3 July 2008, 190–204, 2008.

McKenney, D. W., Hutchinson, M. F., Papadopol, P., Lawrence, K., Pedlar, J., Campbell, K., Milewska, E. M., Hopkinson, R. F., Price, D., and Owen, T.: Customized spatial climate models for North America, B. Am. Meteorol. Soc., 92, 1611–1622, 2011.

Morse, P. D., Burn, C. R., and Kokelj, S. V.: Influence of snow on near-surface ground temperatures in upland and alluvial environments of the outer Mackenzie Delta, Northwest Territories, Can. J. Earth Sci., 49, 895–913, doi:10.1139/E2012-012, 2012.

TCD
8, 1895–1935, 2014

Nelson, F. E. and Outcalt, S. I.: A computational method for prediction and regionalization of permafrost, Arctic Alpine Res., 19, 279–288, 1987.
Nelson, F. E., Shiklomanov, G. N. I., Mueller, G., Hinkel, K. M., Walker, D. A., and Bockheim, J. G.: Estimating active-layer thickness over a large region: Kuparuk River basin, Alaska, USA, Arctic Alpine Res., 29, 367–378, 1997.
Nguyen, T.-N., Burn, C. R., King, D. J., and Smith, S. L.: Estimating the extent of near-surface permafrost using remote sensing, Mackenzie Delta, Northwest Territories, Permafrost Periglac., 20, 141–153, doi:10.1002/ppp.637, 2009.
Nikiforoff, C.: The perpetually frozen subsoil of Siberia, Soil Sci., 26, 61–78, 1928.
Olthof, I., Latifovic, R., and Pouliot, D.: National scale medium resolution land cover mapping of Canada from SPOT 4/5 data, 34th Canadian Symposium on Remote Sensing, Victoria, British Columbia, Canada, 27–29 August, 2013.
Osterkamp, T. E.: The recent warming of permafrost in Alaska, Global Planet. Change, 49, 187–202, doi:10.1016/j.gloplacha.2005.09.001, 2005.
Riseborough, D. W., Wolfe, S. A., and Duchesne, C.: Permafrost Modelling in Northern Great Slave Region Northwest Territories, Phase 1: Climate data evaluation and 1-D sensitivity analysis, Geological Survey of Canada Open File 7333, Ottawa, ON, Canada, 43 pp., 2013.
Roujanski, V. E., Horne, B., Zhang, G., McGuaig, M., Blade, M., and Regular, M.: Warming permafrost temperature at two mine sites in the North Slave Region, Northwest Territories, Canada, in: Proceedings of the Tenth International Conference on Permafrost, vol. 1: International contributions, edited by: Hinkel, K. M., The northern Publisher, 25–29 June 2012, Salekhard, Yamal-Nenets Autonomous District, Russia, 353–358, 2012.
Smith, S. L. and Burgess, M. M.: A Digital Database of Permafrost Thickness in Canada, Geological Survey of Canada Open File 4173, Ottawa, ON, Canada, 38 pp., 2002.
Stevens, C. W., Wolfe, S. A., Gaanderse, A. J. R.: Lithalsa distribution, morphology and landscape associations in the Great Slave Lowlands, Northwest Territories, Geological Survey of Canada Open File 7255, Ottawa, ON, Canada, 34 pp., 2012.
Tape, K., Sturm, M., and Racine, C.: The evidence for shrub expansion in Northern Alaska and the Pan-Arctic, Glob. Change Biol., 12, 686–702, doi:10.1111/j.1365-2486.2006.01128.x, 2006.
Turetsky, M. R., Kane, E. S., Harden, J. W., Ottmar, R. D., Manies, K. L., Hoy, E., and Kasischke, E. E.: Recent acceleration of biomass burning and carbon losses in Alaskan forests and peatlands, Nat. Geosci., 4, 27–31, doi:10.1038/ngeo1027, 2011.

TCD
8, 1895–1935, 2014

Vaughan, D. G., Comiso, J. C., Allison, I., Carrasco, J., Kaser, G., Kwok, R., Mote, P., Murray, T., Paul, F., Ren, J., Rignot, E., Solomina, O., Steffen, K., and Zhang, T.: Observations: Cryosphere, in: Climate Change 2013: The Physical Science Basis. Contribution of Working Group I to the Fifth Assessment Report of the Intergovernmental Panel on Climate Change, edited by: Stocker, T. F., Qin, D., Plattner, G.-K., Tignor, M., Allen, S. K., Boschung, J., Nauels, A., Xia, Y., Bex, V., and Midgley, P. M., Cambridge University Press, Cambridge, United Kingdom, and New York, NY, USA, 317–382, 2013.

Wang, T., Hamann, A., Spittlehouse, D., and Aitken, S. N.: Development of scale-free climate data for western Canada for use in resource management, Int. J. Climatol., 26, 383–397, doi:10.1002/joc.1247, 2006.

Wolfe, S. A., Duchesne, C., Gaanderse, A., Houben, A. J., D'Onofrio, R. E., Kokelj, S. V., and Stevens, C. W.: Report on 2010–2011 Permafrost Investigations in the Yellowknife Area, Northwest Territories, Geological Survey of Canada Open File 6983, Ottawa, ON, Canada, 75 pp., 2011.

Wolfe, S. A., Stevens, C. W., Gaanderse, A. J., and Oldenborger, G. A.: Lithalsa distribution, morphology and landscape associations in the Great Slave Lowland, Northwest Territories, Canada, Geomorphology, 204, 302–313, doi:10.1016/j.geomorph.2013.08.014, 2014.

Woo, M., Lewkowicz, A. G., and Rouse, W. R.: Response of the Canadian permafrost environment to climatic change, Phys. Geogr., 13, 287–317, 1992.

Yi, S., Woo, M.-K., and Arain, A. M.: Impacts of peat and vegetation on permafrost degradation under climate warming, Geophys. Res. Lett., 34, L16504, doi:10.1029/2007GL030550, 2007.

Yoshikawa, K., Bolton, W. R., Romanovsky, V. E., Fukuda, M., and Hinzman, L. D.: Impacts of wildfire on the permafrost in the boreal forests of interior Alaska, J. Geophys. Res., 107, 8184, doi:10.1029/2001JD000438, 2003.

Zhang, T., Barry, R. G., Knowles, K., Heginbottom, J. A., and Brown, J.: Statistics and characteristics of permafrost and ground ice distribution in the Northern Hemisphere, Polar Geogr., 23, 147–169, 1999.

Zhang, Y.: Spatio-temporal features of permafrost thaw projected from long-term high resolution modeling for a region in the Hudson Bay Lowlands in Canada, J. Geophys. Res.-Ea. Surf., 118, 542–552, doi:10.1002/jgrf.20045, 2013.

TCD
8, 1895–1935, 2014

Zhang, Y., Li., C., Trettin, C. C., Li, H., and Sun, G.: An integrated model of soil, hydrology and vegetation for carbon dynamics in wetland ecosystems, Global Biogeochem. Cy., 16, 1061, doi:10.1029/2001GB001838, 2002.

Zhang, Y., Chen, W., and Cihlar, J.: A process-based model for quantifying the impact of climate change on permafrost thermal regimes, J. Geophys. Res., 108, 4695, doi:10.1029/2002JD003354, 2003.

Zhang, Y., Chen, W., Smith, S. L., Riseborough, D. W., and Cihlar, J.: Soil temperature in Canada during the twentieth century: complex responses to atmospheric climate change, J. Geophys. Res., 110, D03112, doi:10.1029/2004JD004910, 2005.

Zhang, Y., Chen, W., and Riseborough, D. W.: Temporal and spatial changes of permafrost in Canada since the end of the Little Ice Age, J. Geophys. Res., 111, D22103, doi:10.1029/2006JD007284, 2006.

Zhang, Y., Chen, W., and Riseborough, D. W.: Disequilibrium response of permafrost thaw to climate warming in Canada over 1850–2100, Geophys. Res. Lett., 35, L02502, doi:10.1029/2007GL032117, 2008.

Zhang, Y., Li, J., Wang, X., Chen, W., Sladen, W., Dyke, L., Dredge, L., Poitevin, J., McLennan, D., Stewart, H., Kowalchuk, S., Wu, W., Kershaw, G. P., and Brook, R. K.: Modelling and mapping permafrost at high spatial resolution in Wapusk National Park, Hudson Bay Lowlands, Can. J. Earth Sci., 49, 925–937, doi:10.1139/E2012-031, 2012.

Zhang, Y., Wang, X., Fraser, R., Olthof, I., Chen, W., Mclennan, D., Ponomarenko, S., and Wu, W.: Modelling and mapping climate change impacts on permafrost at high spatial resolution for an Arctic region with complex terrain, The Cryosphere, 7, 1121–1137, doi:10.5194/tc-7-1121-2013, 2013.

TCD
8, 1895–1935, 2014

Table 1. Land-cover types classified using SPOT satellite.

Code	Name	Type description
D	Deciduous – medium to high density	Cold deciduous forest, closed tree canopy (crown closure 25–60 %), small coniferous-herb understory.
M	Mixed – medium to high density	Mixed cold deciduous-needle leaved evergreen forest (crown closure 25–50 %).
C1	Coniferous – high density	Sub-polar needle leaved evergreen forest (crown closure > 75 %).
C2	Coniferous – medium density	Sub-polar needle leaved evergreen forest, lichen-shrub understory.
C3	Coniferous – low to medium density	Sub-polar needle leaved evergreen forest, low-medium density, shrub-lichen understory.
C4	Sparse coniferous-shrub cover	Sparse needle leaved evergreen forest, herb-shrub cover understory.
C5	Spruce lichen bog	Wetland type feature that supports lichens and treed bogs.
W	Wetland or fen	Treed or herbaceous wetland with water table near or above the surface.
S	Erect shrubs	Tall shrubs or dense low shrubs.
SH	Shrub-herb mixture	Mixture of herbs and shrubs.
H	Herbs	Herb dominated (but not fens)
L	Low vegetation or lichen barren	Low- or non-vegetated area (but not roads or recently disturbed areas).
R	Rock outcrop	Rock outcrops with sparse vegetation.
U	Disturbed area	Recently disturbed areas (not modelled)
O	Roads	Roads (not modelled)
W	Water	Lakes, rivers, or ponds (not modeled)

TCD
8, 1895–1935, 2014

Table 2. Probability parameters of organic layer thickness and the number of ground-types for each land-cover type estimated using field observations.

Type code	Observation sites	Probability parameters (cm) a	μ	s	R^2	Number of ground-types
D	9	−0.55	2.0	5.0	0.985	5
M	16	−0.5	5.0	8.5	0.968	6
C1	15	0.1	11.7	2.2	0.971	5
C2	14	−0.15	17.5	11.0	0.988	7
C3	7	0	18.0	7.5	0.964	6
C4	6	0.05	36.0	12.0	0.973	7
C5	20	−0.07	82.0	24.5	0.981	8
W	25	−0.5	20.5	20.0	0.977	7
S	19	−0.35	11.0	9.0	0.957	7
SH	11	−0.35	9.0	8.5	0.999	7
H	6	−0.5	15.5	6.0	0.928	7
L	4	−0.01	0.01	1.1	0.961	3
R	8	–	–	–	–	1

R^2 is the square of the correlation coefficient between the fitted and observed relative cumulative frequency.

TCD
8, 1895–1935, 2014

Table 3. Hydrological parameters defined for different land-cover types.

Type code	Ground inflow		Surface outflow		Ground outflow		Snow drifting parameter
	WT_{ig}	F_{ig}	WT_{os}	F_{os}	WT_{og}	F_{og}	
D	100	0.1	0	0.1	50	0.05	0
M	100	0.1	0	0.1	30	0.05	$-0.03L$
C1	–	–	10	0.1	30	0.05	$-0.05L$
C2	–	–	0	0.1	30	0.05	$-0.03L$
C3	–	–	0	0.1	30	0.05	0.00
C4	–	–	0	0.1	30	0.02	0.00
C5	60	0.1	0	0.1	20	0.05	0.00
W	20	0.05	−10	0.05	–	–	0.00
S	–	–	0	0.1	20	0.1	$-0.10L$
SH	–	–	0	0.1	15	0.1	$-0.05L$
H	–	–	0	0.1	5	0.1	0.00
L	–	–	0	0.1	20	0.1	$0.1\text{-}0.1L$
R	–	–	0	0.5	–	–	$0.2–0.1L$

WT_{ig} is the lowest water table (cm below the surface) for beginning lateral ground inflow. WT_{os} and WT_{og} are the highest water table (cm below the surface) for beginning lateral surface and ground outflows, respectively. F_{ig} is the rate of ground inflow (day^{-1}). F_{os} and F_{og} are the rates of surface and ground outflows, respectively (day^{-1}). Detailed description of these parameters can be found in Zhang et al. (2002, 2012).
–: Assuming no lateral flows.
L is for leaf area indices in peak growing season.

TCD
8, 1895–1935, 2014

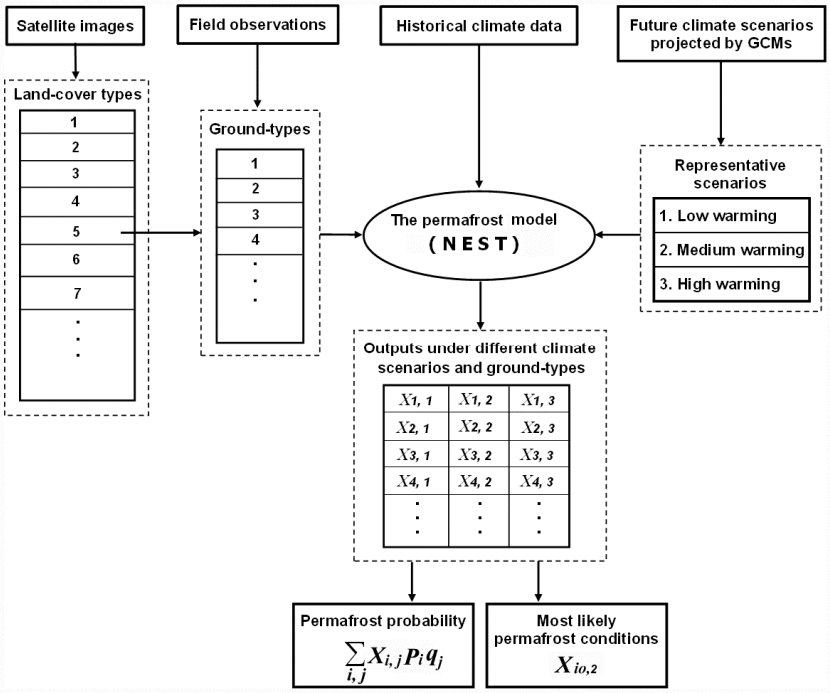

Fig. 1. The scheme of the new permafrost mapping approach. A land-cover map classified from satellite images is used to represent the general land conditions and to improve the spatial resolution. For each land-cover type, the probability of different ground conditions is estimated based on field observations. A process-based permafrost model (NEST) was used to calculate the evolution of permafrost for each ground-type under three representative climate change scenarios generated by general circulation models (GCMs). From the model outputs, the probability of permafrost occurrence and the most likely permafrost conditions are determined. In the above scheme, $X_{i,j}$ is the model output based on ground-type i and climate scenario j. p_i is the probability of ground-type i, and q_j is the probability of climate scenario j. io is the most probable ground-type.

TCD
8, 1895–1935, 2014

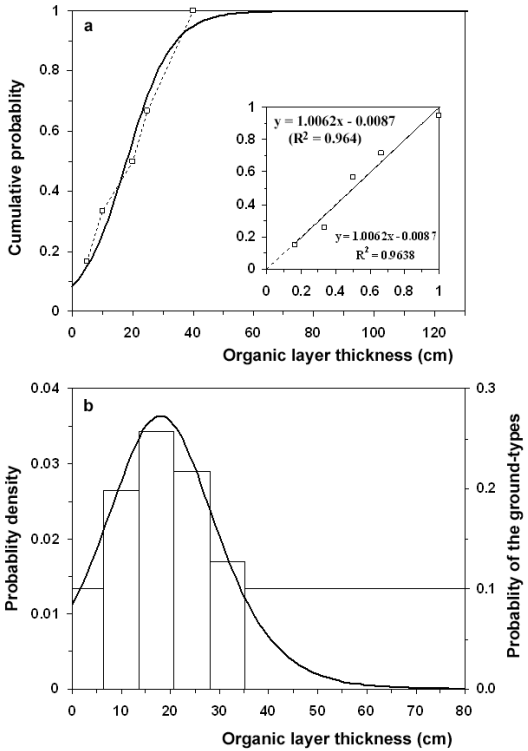

Fig. 2. An example of determining the probability distribution of organic layer thickness for a land-cover type (C3, coniferous forest – low to medium density). **(a)** Fitting the observed relative cumulative frequency (the dash curve) with a modified logistic function (the bold curve). The inset shows the scatter graph comparison and linear regression for the fitting. **(b)** The probability density (the bold curve), and the distribution of the ground-types and their probabilities (the rectangle boxes).

TCD
8, 1895–1935, 2014

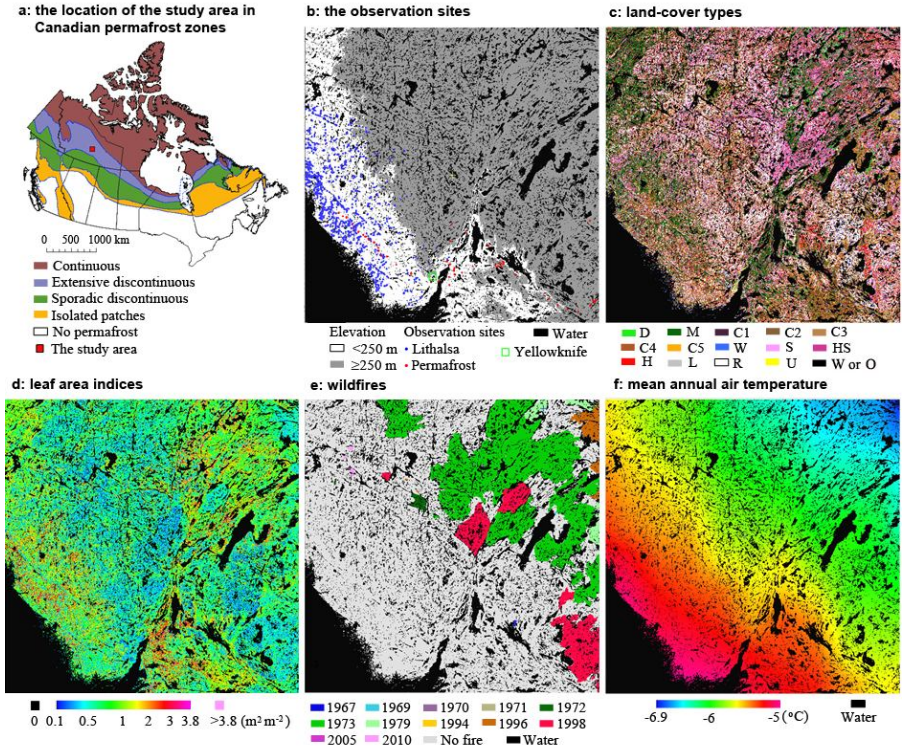

Fig. 3. (a) the location of the study area in Canadian permafrost zones (Heginbottom et al., 1995), **(b)** the observation sites and the two regions divided based on elevation 205 m a.s.l., and the distributions of **(c)** land-cover types, **(d)** leaf area indices, **(e)** wildfires, and **(f)** thirty-year (1971–2000) mean air temperature in the study area.

TCD
8, 1895–1935, 2014

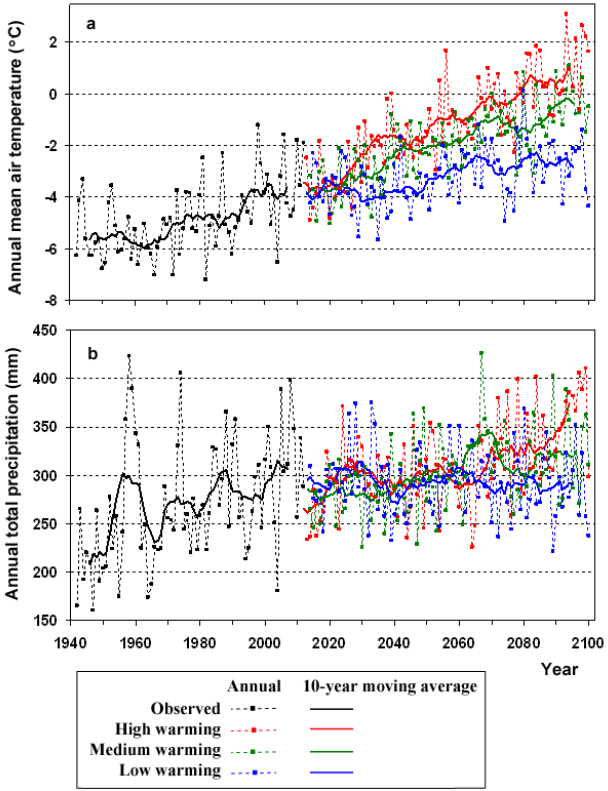

Fig. 4. The historical climate trends and the selected three scenarios for the 21st century for **(a)** annual mean temperature and **(b)** annual total precipitation. The historical climate is observed at Yellowknife airport climate station. The low, medium and high warming scenarios were generated by CCCma (B1), CCCma (A1B) and MIROC (A1B), respectively. More details about the data and the climate models can be found at the World Data Center for Climate (http://mud.dkrz.de/wdc-for-climate/).

TCD
8, 1895–1935, 2014

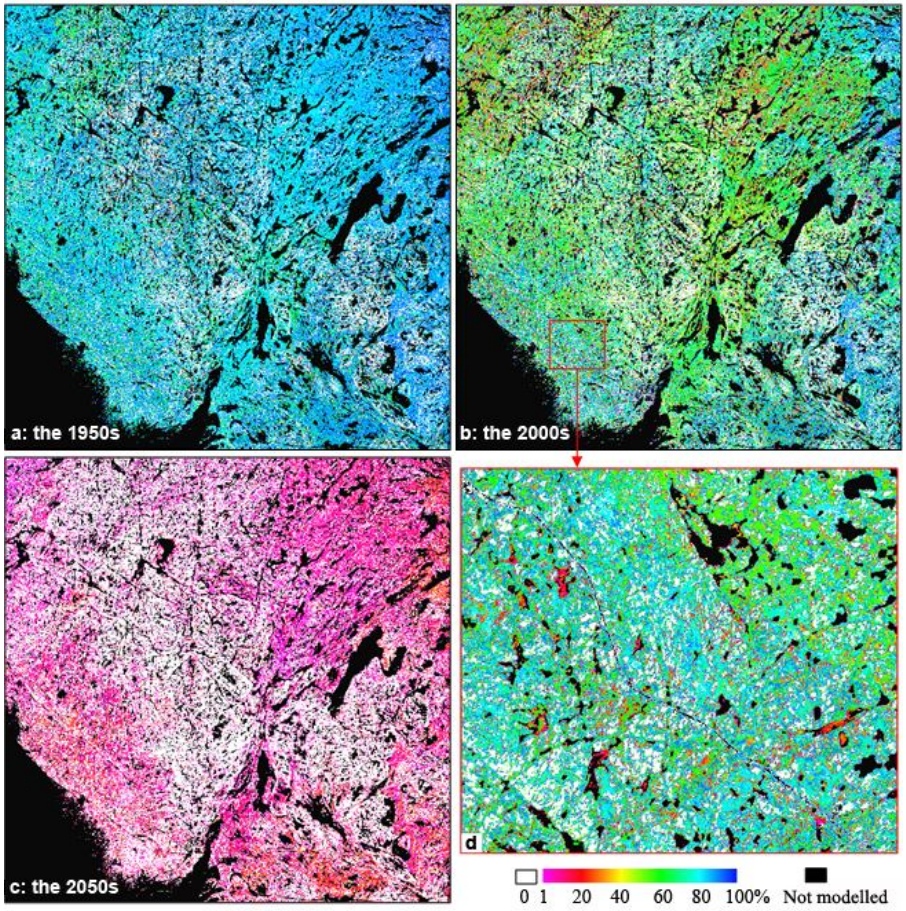

Fig. 5. Modelled permafrost probability distributions in the 1950s, 2000s and 2050s (**a**, **b**, and **c**, respectively). Panel **(d)** shows an enlarged area in panel **(b)**.

TCD
8, 1895–1935, 2014

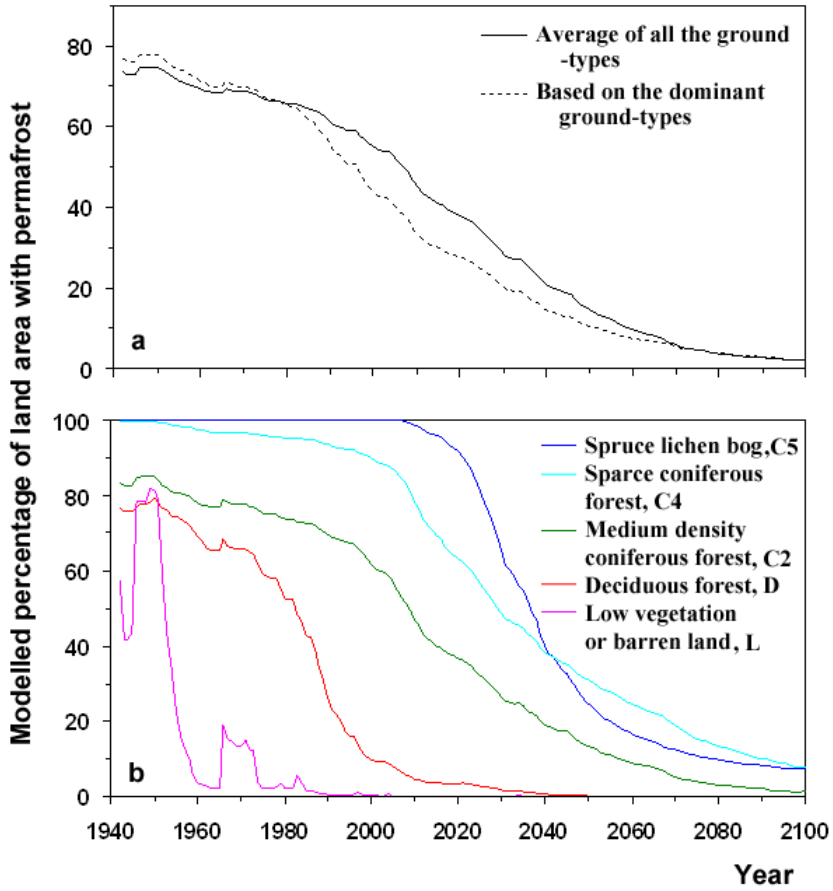

Fig. 6. The modelled temporal changes of permafrost probability **(a)** for the entire study area and **(b)** for five selected land cover types in this area.

TCD
8, 1895–1935, 2014

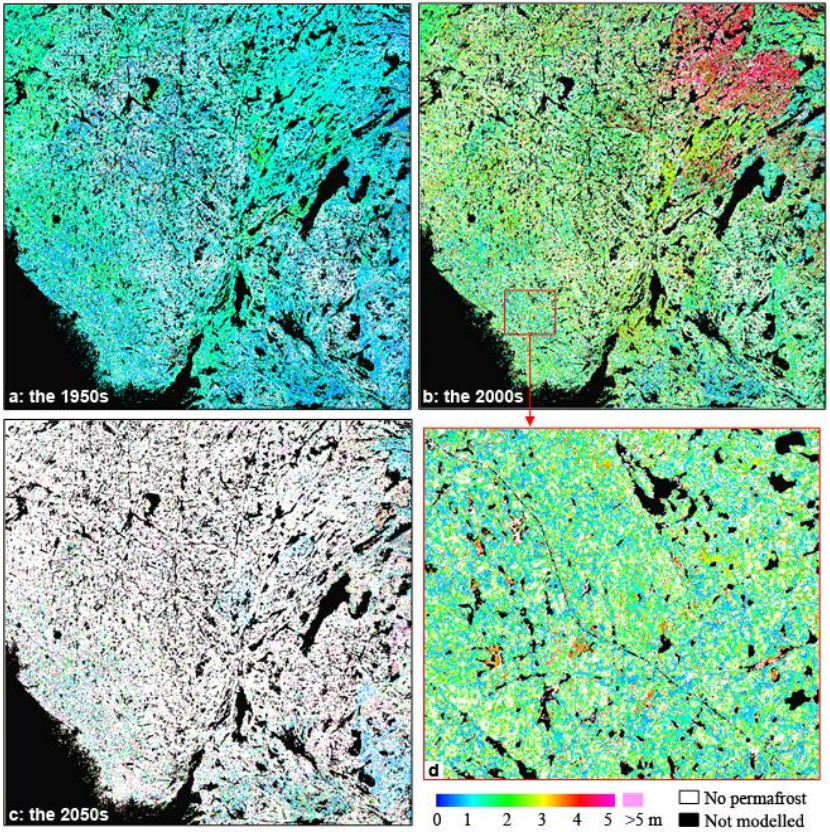

Fig. 7. Modelled most likely active-layer thickness in the 1950s, 2000s and 2050s (**a**, **b**, and **c**, respectively). Panel **(d)** shows an enlarged area in panel **(b)**. This figure also shows the most likely distribution of permafrost (white color for non-permafrost areas, and the other colours (except black) for areas with permafrost).

TCD
8, 1895–1935, 2014

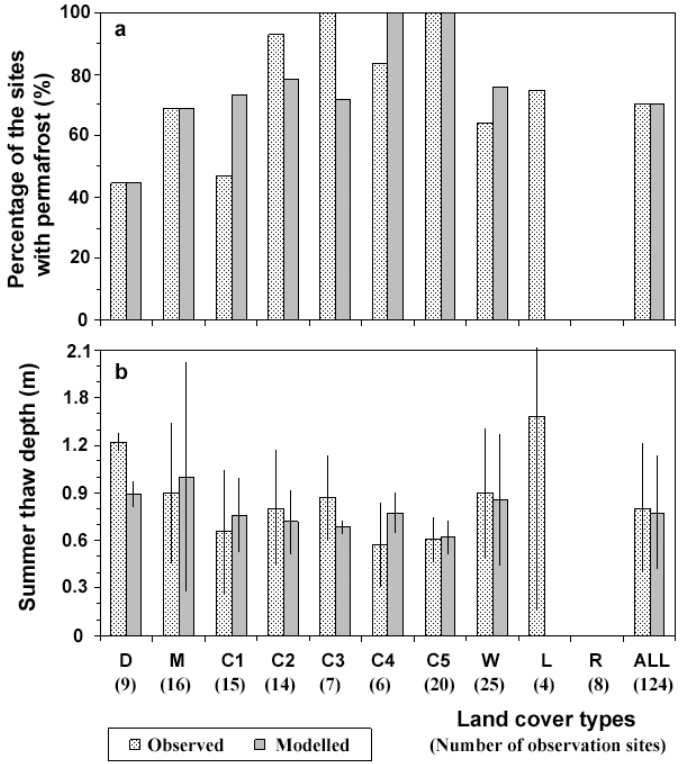

Fig. 8. Comparisons of observed and modelled **(a)** percentage of the sites with permafrost and **(b)** the average and standard deviation of summer thaw depths for each land cover type. The numbers in brackets below the *x* axis are the numbers of observation sites. The average or the standard deviation of summer thaw depths were calculated based on the sites with permafrost (observed or modelled). The land cover types S, SH and H were not shown because there were no field observations for these three types in the study area.

TCD
8, 1895–1935, 2014

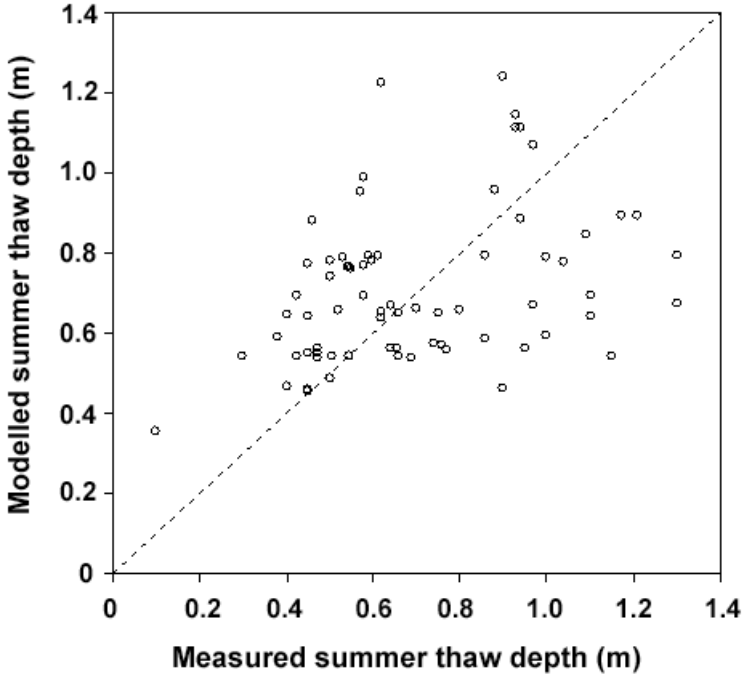

Fig. 9. Comparison between the modelled and measured summer thaw depths. There are 71 observation sites where both observation and the model show the existence of permafrost. The correlation coefficient is 0.365 (n = 71).

TCD
8, 1895–1935, 2014

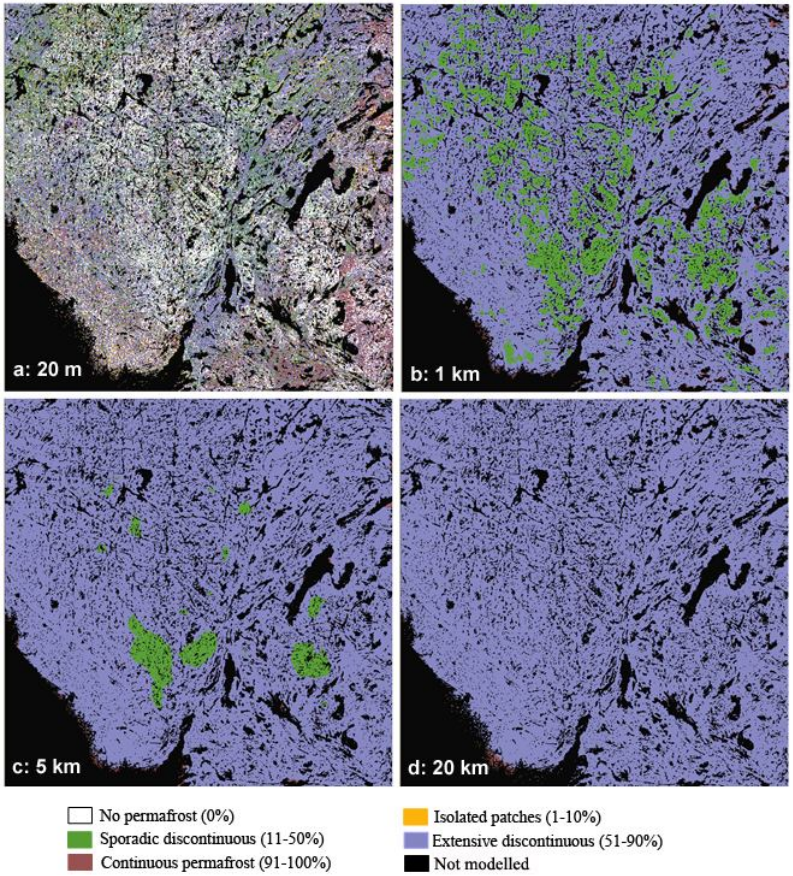

Fig. 10. The effects of spatial resolution (shown in the panels) on permafrost zonal distributions. These maps were produced by dividing permafrost probability in the 2000s (Fig. 5b) into five zones and then re-sampled to different spatial resolutions.

TCD
8, 1895–1935, 2014